Planetary and Space Science 86 (2013) 57–65

Contents lists available at ScienceDirect

Planetary and Space Science

journal homepage: www.elsevier.com/locate/pss

Utility of laser altimeter and stereoscopic terrain models: Application to Martian craters

Stuart J. Robbins [a,*], Brian M. Hynek [b]

[a] Laboratory for Atmospheric and Space Physics, University of Colorado at Boulder, 3665 Discovery Dr., Boulder, CO 80309, United States
[b] Laboratory for Atmospheric and Space Physics, Department of Geological Sciences, University of Colorado at Boulder, 3665 Discovery Dr., Boulder, CO 80309, United States

ARTICLE INFO

Article history:
Received 8 December 2012
Received in revised form
6 June 2013
Accepted 21 June 2013
Available online 29 June 2013

Keywords:
Mars
Mars craters
Remote sensing
Topography
MOLA
HRSC

ABSTRACT

The use of numerical datasets of the same type derived from remote sensing instruments is often treated as equivalent in value and utility, within the limits of their spatial resolution. Surface topography is a good example of this. We used gridded digital terrain models (DTMs) derived from both laser altimetry and stereo pairs as well as the original laser data points to quantify the topography of impact craters, which have well-studied morphometry. The primary purpose was to test the accuracy of laser data given an image-based DTM with approximately a factor of 10 better spatial resolution; we used the Mars Orbiter Laser Altimeter and High-Resolution Stereo Camera datasets for this work. We found that the ability to derive accurate topographic information in laser altimetry diminished well before the ability to visually resolve the feature in the dataset, but we also found that laser point and gridded data-based results were in good agreement down to their resolution limits. Relative to the image-based DTM, pixel-for-pixel, the laser data were more useful in their ability to visibly resolve the impact craters. This work has implications for remote sensing in general, but specifically the application to limited sources of data for planetary surface topography, such as Mercury where the northern hemisphere topography is being measured with a laser altimeter but the southern hemisphere topography is based only on stereo pairs.

1. Introduction

Extraplanetary projectiles are by far the primary exogenic force that modifies planetary surfaces across the solar system, and the vast majority of solid bodies are covered with their end result: impact craters. Studying these surfaces relies upon an accurate understanding of impact craters and their properties, leading to a history of their investigation spanning over 400 years. Besides location and diameter, the primary morphometric feature measured is crater rim-to-floor depth.

Determining this seemingly simple property is challenging, and it also has a long history. Two techniques based on imagery were used early in planetary studies, and they are still in use today: photoclinometry and shadow measurements (e.g., Chapman and Jones, 1977; Pike, 1976, 1977, 1980, 1988; Davis and Soderblom, 1984). Photoclinometry requires precisely knowing the light angle on a surface and assuming a uniform reflectance or a known varying reflectance. A three-dimensional reconstruction is based on the different shading, where a slightly brighter area would indicate a surface aimed more towards the light, and a darker area would indicate a surface aimed away from the light—the exact shade indicates the amount of relative tilt. Shadow length requires a model of the crater shape. It relies on knowing the sun angle relative to the surface and observing how far the shadow cast by the crater rim extends into the modeled crater cavity below.

These two techniques have been used by countless researchers on tens of thousands of craters, but they are not a direct measurement of the depth properties. For a more direct measurement where *in situ* surveying is not possible, one needs to use elevation data from remote sensing techniques. Explored in this work is the relative accuracy of two types of elevation measurements—laser altimetry and digital terrain models (DTMs) from stereo pairs. Their finite resolution was examined as applied to the study of Martian crater properties from a recently released global Martian crater database (Robbins and Hynek, 2012a). Since the DTMs are of much higher spatial resolution than the laser altimetry, in this work we assume that the stereo-derived DTMs represent the "true" elevation data in comparison with the laser results (see Section 4.5). While Section 2 describes these two different datasets and Section 3 describes how the topography values were determined, Section 4 contains a detailed comparison between the two datasets for nearly 1000 craters. Section 5 summarizes these results and provides recommendations for future work.

* Corresponding author. Tel.: +1 303 918 5589.
E-mail addresses: stuart.robbins@colorado.edu (S.J. Robbins), hynek@lasp.colorado.edu (B.M. Hynek).

0032-0633/$ - see front matter © 2013 Elsevier Ltd. All rights reserved.
http://dx.doi.org/10.1016/j.pss.2013.06.019

2. Overview of datasets

2.1. Mars Orbiter Laser Altimeter and derived point and gridded data products

Mars Global Surveyor included the Mars Orbiter Laser Altimeter experiment (MOLA) (Zuber et al., 1992; Smith et al., 2001). The instrument operated for 2 years by measuring the light-time-return of a 1.064 μm laser pulse sent from the craft, reflected off the surface, and returned to the instrument. It had an 8 ns pulse frequency of 10 Hz which, based on the average orbital speed, resulted in an along-track footprint spacing of ~300 m while each footprint was ~160 m in diameter due to spreading; inaccuracies in spacecraft orbit reconstruction result in uncertainties of ~100 m of where the footprint is centered (Neumann et al., 2003a). The return signal itself was an average of the light-time-return over the entire footprint area. The across-track spacing varied significantly with latitude but was generally <2 km at the equator and much smaller closer to the poles due to the spacecraft's near-polar orbit (because it was near polar and not polar, measurements poleward of $\pm 88^\circ$ latitude were not taken). Vertical accuracy is ~1 to 10 m due to spacecraft orbit and instrument measurement uncertainties (Smith et al., 2001). However, this does not take into account the fact that the footprint is ~160 m in diameter and therefore represents an average over what may be a significant topographic difference. For example, a footprint with an edge on a crater rim crest with the remainder extending into a fresh crater cavity with a slope of 30° would have a topographic range of 92 m; yet, the data point returned would just be the average of that range, depressing the rim height.

We can explore the theoretical quality of the laser point data for measuring crater rims via Monte Carlo simulations. For this exercise, model craters between 3 km and 20 km in diameter were simulated along with simulated MOLA tracks overprinted. The simulation used the spacing and point size described in the above paragraph with randomized track longitudes with a mean of 2 km separation to simulate the equator. The investigation is how many points would be expected to fall directly "on" the crater rim. Since each spot size is ~160 m and crater rims, in practice, are not point locations, we define the rim to be 1.0% of the crater diameter in width, e.g., for a simulated 3-km-diameter (1.5-km-radius) crater, then the rim would be 1.485–1.515 km from the crater center. We then ran the simulation 5000 times. We found that for $D=3$ km craters, there were only 2.2 ± 1.6 laser points with centers that fell within that narrow 30-m annulus. It was not until $D=6$ km craters that twice as many points as the crater diameter were on the rim: 12.1 ± 3.1. For $D=10$ km craters, the number of points is 35.2 ± 5.1, and for $D=20$ km, the points on the rim are 144 ± 13. While the exact values change based on the mean across-track spacing and rim annulus definition used, the overall trend is the same. For craters $D<10$ km, the number of points on this defined rim annulus is <30, and for craters $D=3$ km, the number of points is generally <5. An alternative way to explore this is to ask what the probability is that a track will have a laser point both in the center of the crater (defined for this as the inner 2% of the crater) and within the above-defined rim annulus. When the Monte Carlo simulation is run with these constraints, craters $D=3$ km have only a 3.3% chance of having a laser shot in the middle and on the rim, craters $D=5$ km have a 10% chance, $D=10$ km have a 33% chance, and $D=20$ km have a 63% chance. These simulation results support our conclusions later in this work that craters $D<10$ km tend to be shallower in MOLA than with higher-resolution stereo DTMs due to few points directly on the rim.

The MOLA instrument returned approximately 595 million topographic measurements that now form its primary dataset (Neumann et al., 2003a, 2003b). The point data represent the most original form, being a vector dataset unconstrained by pixel gridding. It is available publicly as the MOLA Precision Experiment Data Records (PEDR). Meanwhile, because of the large file size represented by the 595 million points (~14.5 GB of data in ASCII

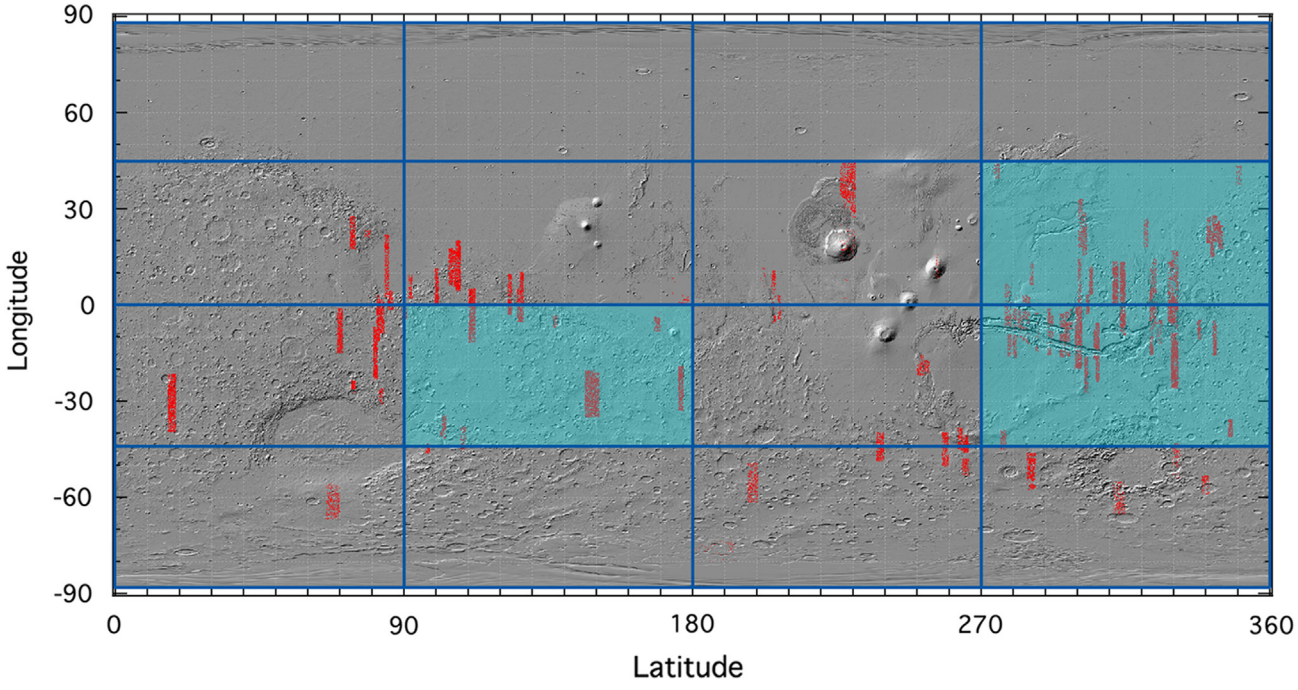

Fig. 1. Shaded relief basemap of Mars (Smith et al., 2001). Overlaid in red dots are craters from Robbins and Hynek (2012a) that fall within the latitude and longitude range of all 124 HRSC DTMs at 50 m/px scale. Blue grid overlaid are divisions of 1/128° MOLA MEGDR data, while shaded in turquoise are the three images that contain craters with diameters $D \geq 3$ km with HRSC DTM and MOLA overlap that were analyzed in this study. (For interpretation of the references to color in this figure caption, the reader is referred to the web version of this article.).

format), many who want to use MOLA data for large studies cannot do so due to physical and computational limitations of modern computers.

Most people instead use the data in a gridded, raster format, available freely in 1/4°, 1/16°, 1/32°, 1/64°, and 1/128° products as the Mission Experiment Gridded Data Records (MEGDR). (Up to 1/512° gridded data are available at high latitudes, $\gtrsim 75°$.) The 1/128° data are separated into 16 individual images of the planet, covering 90° in longitude and 44° in latitude (Fig. 1), and they only require ~130 MB of disk space each. The pixel size of the 1/128° product, at the equator, is approximately 463 m on each side. At this scale, the original PEDR data tracks are non-uniform, and pixels may have anywhere from 0 to 20 points that went into it (the ones with 0 PEDR points were interpolated, which occurred in 43.6% of pixels—i.e., 43.6% of the pixels have no PEDR points within them; >99% of pixels have ≤4 PEDR points within their 1/128° size).

The laser altimeter is the most direct method at this time for determining topographic values, and versions of it are currently in operation around both Mercury and Luna (Cavanaugh et al., 2007; Chin et al., 2007). Ergo, understanding the limitations of their data returns is important for a variety of studies on multiple planets. For the work described in this paper, both PEDR and 1/128° MEGDR data were used and compared.

2.2. High-Resolution Stereo Camera and derived digital terrain models

Mars Express, in orbit around Mars since 2003, contains the first camera built for extraterrestrial remote sensing with the specific purpose of obtaining high-spatial-resolution stereoscopic pairs for the purpose of creating digital terrain models (DTMs). The camera, the High-Resolution Stereo Camera (HRSC), is capable of up to 10 m/pix imaging of the Martian surface in the originally designed periapsis orbit of 250 km (Neukum and Jaumann, 2004; Jaumann et al., 2007; Gwinner et al., 2010). *Mars Express* is on an elliptical orbit with a periapsis approx. 277–298 km and apoapsis of 10,114–10,107 km, meaning that the actual spatial resolution varies from image-to-image and also can vary over a single image (the original planned 250 km periapsis was never reached, so the original design of 10 × 10 m/pix could not be achieved). On the craft, images are compressed via a lossy JPG algorithm and then sent to Earth. The raw data (Level-1) are radiometrically calibrated, corrected for geometric distortion, and then map projected (Level-3) (Jaumann et al., 2007).

For purposes of DTM creation, the Level-3 data are resampled at 12.5 m, 25 m, or 50 m/px, and these are processed into 50 m, 75 m, or 100 m/px DTMs (higher-resolution images may be down-sampled depending on quality). Gwinner et al. (2010) provides a detailed description of the DTM creation. In short, detailed pointing and camera data are used to align image pairs. Points between pairs are matched and interpolated to produce a dense network of 3D points based on the different viewing geometry. These points are tied to the MOLA PEDR database and iterated to minimize offsets and improve consistency. The final image is then output.

For the work described in this paper, only the highest-resolution 50 m/px data were used (1/1183° per pixel, ~10 × the MOLA MEGDR), and these are estimated to have a vertical accuracy of ~10s m (Gwinner et al., 2010). As of late 2012, 124 DTMs at this scale were publicly available. The distribution of images is far from uniform across the planet, as shown in Fig. 1. They are also tilted relative to lines of latitude and longitude, meaning that the craters within the full latitude and longitude extent cannot be studied with these image data because there will not be image data there. Craters that were in these images were examined in HRSC data, while only those in three of the 1/128° MOLA MEGDR images were studied for this work. The craters were a subset of the Robbins and Hynek (2012a) crater database, comprising 57.1% of the craters with overlap in both topography datasets.

3. Method of measuring crater topographic properties

Robbins and Hynek (2012a) published the first and only global Martian crater database with a complete sampling of craters as small as 1-km-diameter (D); it contains 384,343 craters $D \geq 1$ km. Of those, 79,723 are $D \geq 3$ km, and we attempted to derive topographic properties of these craters with MOLA MEGDR. The method of that work, in brief, was to create three polylines, one each representing the high points along the crater rim, an estimate of the surrounding surface elevation, and the deepest points of the crater floor; this is illustrated in Fig. 2B. The mean and standard deviation of the topographic values at each vertex were saved, and from those, properties such as rim-floor depth could be derived. The number of points used was somewhat diameter-dependent but was set to a maximum of 250; roughly, the average number of rim points was 46 ± 37, surface points 101 ± 54, and floor points 29 ± 33 ($\pm$ values are 1σ, and there were no polylines with <3 points and none with negative points).

In the time since that work, we have developed a semi-automated revision to that code. It is still based on the researcher manually creating polylines (Fig. 2C). The first identifies the rim while the second and third are an enclosed shape that identifies the surrounding surface and the crater floor. The computer then examines all points enclosed by the surface shape, fits a plane, and takes the average and standard deviation of that plane (it can fit other models, but a plane was used for this work). The points within the floor shape are then saved, and the mean and standard deviation are calculated. The code will then remove all points above this mean and compute and save the new mean and standard deviation as the estimate for the floor depth. The rim is then analyzed. First, the algorithm snaps the vertices to the DTM grid, removes duplicate points, and interpolates between them. Then, radially from the crater center, points within a $\pm$buffer (user-set but scales with crater diameter) are searched for the local high for each vertex along the rim. The mean and standard deviation are saved, and, as with the floor, the points below the mean are rejected and the final mean and standard deviation saved for the estimate of the rim height. An additional option (used in this work) removed MEGDR data that had zero corresponding PEDR points, i.e., it was purely interpolated. The result is shown in Fig. 2D. This code can operate using either or both gridded data (MEGDR, DTM) and/or point data (PEDR) from the same three polylines so that the same analysis can be done in both datasets without duplicating effort on the part of the researcher. The polylines are saved so changes to the code can be easily made and re-run without duplicated manual work effort. The code is also easily modified for use on other spheroids such as Mercury or Luna.

To help validate the new code, we obtained a synthetic DTM and MOLA-like dataset used in Stewart and Valiant (2006) (courtesy of S. Stewart). We performed the same analysis described above on the synthetic dataset. The results were almost identical to the true values of the synthetic craters except for a systematic ≈4% suppression of crater depth found from our technique versus what the craters should have been. This is consistent with an ideal vector shape with a sharp rim being smoothed out when rasterized into a DEM and finite laser tracks. It is also consistent with artifacts that we discuss in later sections.

This new code has several advantages over that used by Robbins and Hynek (2012a). First, the semi-automated nature allows for more consistent results when faced with small

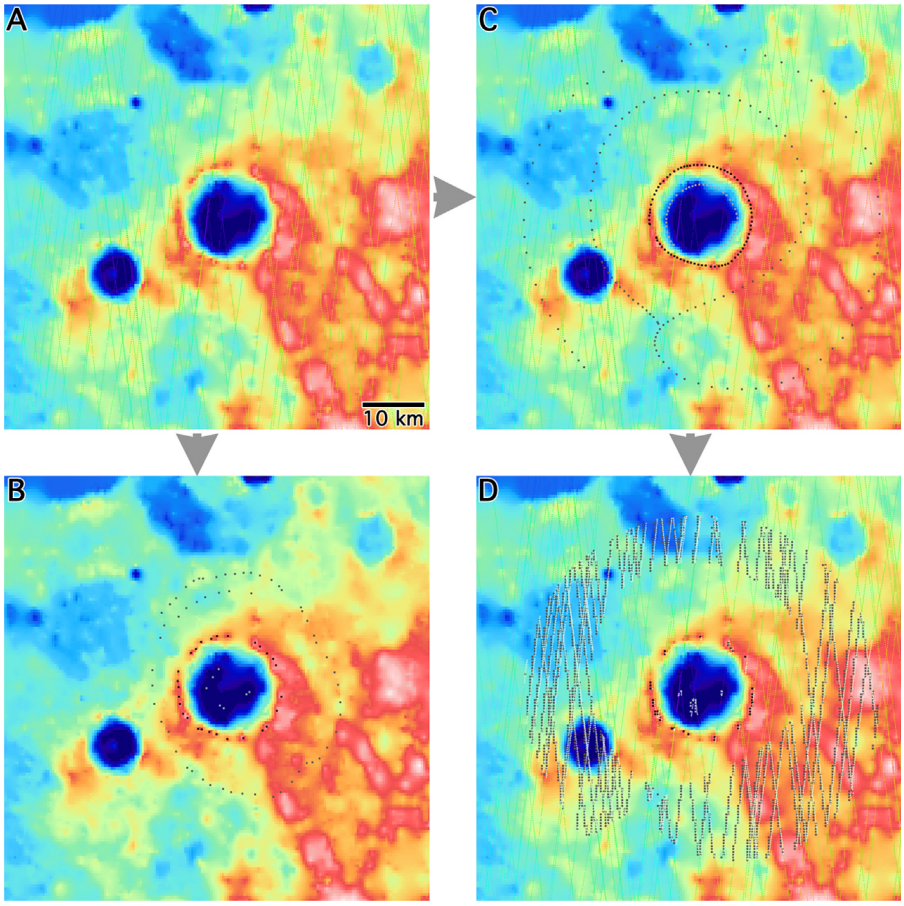

Fig. 2. An example 16.6-km-diameter crater (Panel A) measured with both topography codes—the original (Panel B) from Robbins and Hynek (2012a), and the revision used in this study (Panels C and D). In all panels, background gridded data are MOLA MEGDR set so blue is low and red-white is high elevation. Black squares are sampled rim pixels, dark gray are sampled surrounding surface, and light gray are sampled floor. In Panels A, C, and D, the lines of color are MOLA PEDR where purple is low and red is high (different color scheme so they are visible against MEGDR). In Panel C, the initial lines are drawn, and in Panel D, the automated code has run, per the description in Section 3. Panel D also shows circles with a white border, and these are the PEDR points that were selected by the code based on the manual input. In the original version, the rim-floor depth was 0.98 ± 0.10 km, while in the revised the MEGDR rim-floor depth is 1.05 ± 0.06 km and PEDR is 1.05 ± 0.06 km (identical with each other and within the standard deviation of the original). If the MEGDR points without PEDR points had not been removed from Panel D's processing, the rim-floor depth would be 1.00 ± 0.07 km.

differences between different markings of the same crater (i.e., different researchers or the same researcher multiple times for a consistency test). Second, the code selects the highest points along the rim and the lowest points in the floor much faster than is humanly possible. Third, the radial search for the rim allows for less needed accuracy (or manual dexterity) on the part of the researcher. Fourth, the use of areas of points rather than selecting only points at vertexes of a polyline permits several orders of magnitude more points to be used for more robust results. Finally, the code has the option to use nearest-neighbor searches for the rim to allow the point analysis alongside the gridded analysis.

To be more specific with the fourth benefit, the number of points used to quantify each crater's depth increased significantly with this revised topographic code. The results are highly diameter-dependent, but for comparison sake with the original code, the averages are quoted again with $\pm 1\sigma$ (number of points used was not negative but there were many more small craters than large, lowering each average). For MEGDR analysis, the rims had an average of 27 ± 30 points used, surrounding surface was $5{,}200 \pm 23{,}000$, while the floors were 29 ± 134. Since the new code uses a number of points that is more strongly a function of diameter, a power law can be fit such that the number of points N used is a function of crater diameter D ($N = \alpha \cdot D^{\beta}$). For this MEGDR analysis, the rims had fit parameters $\alpha = 2.3$, $\beta = 1.0$; the surfaces $\alpha = 23$, $\beta = 1.8$; and the floors $\alpha = 0.10$, $\beta = 1.8$.

4. Results

4.1. Numbers of craters with discernable depths

The Robbins and Hynek (2012a) crater database has 384,343 craters $D \geq 1$ km and, of those, 79,723 were $D \geq 3$ km; in that work, 66,744 (83.7%) of the $D \geq 3$ km craters were considered to overlap MOLA MEGDR data sufficiently to have depths computed (were considered "analyzable"). The fraction analyzable was diameter-dependent, where larger craters were nearly 100% analyzable in the MOLA data, and craters smaller than ~7 km fell significantly below 100% (Fig. 3).

The work here is not a complete re-analysis of those global results, but rather it is focused on 3/16ths of the planet where approximately 57% of the craters covered by the 50 m/px HRSC DTMs exist (Fig. 1). Within these regions (3/16ths of Mars), 24,177 craters $D \geq 3$ km are present and they were re-examined with both MOLA MEGDR and PEDR as described in Section 3. These regions also have 98,026 craters $D \geq 1$ km, which was our cut-off for HRSC DTMs (a larger diameter cut-off of 3 km is necessary for the MOLA analysis). Of those 98,026 craters, a subset of 1749 craters $D \geq 3$ km (7.2% the total) are contained within the latitude/longitude range of the HRSC DTMs studied in this work (and so can be directly compared with MOLA-based results), while 6806 are $D \geq 1$ km (6.9% of the total).

The fraction of craters that could be analyzed in these regions is illustrated in Fig. 3. A steady ~90% of craters $D \gtrsim 11$ km were deemed to have sufficient coverage in MOLA data to have depths computed. For smaller diameters, the ability to actually resolve craters in MOLA data diminishes. The fraction is below 50% for craters $D \lesssim 3.8$ km. With HRSC data, the baseline fraction of craters that has HRSC coverage in these regions is approximately 7% (see previous paragraph). The fraction of craters not analyzable drops below this for $D \lesssim 3.0$ km. The fraction is below 50% ($\lesssim 3.5\%$ of the total catalog) for craters $D \lesssim 1.2$ km.

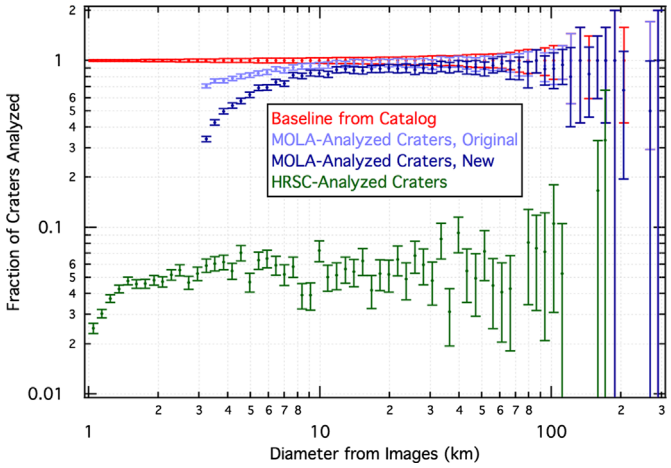

Fig. 3. Fraction of measured craters within the 3/16ths of the planet shown in Fig. 1 as a function of diameter ($2^{1/8}D$ multiplicative bins). The craters in the Robbins and Hynek (2012a) global catalog, selected for the regions shown in Fig. 1 are in red with $\pm\sqrt{N}$ uncertainty bars attached, and the fraction of craters measured in Robbins and Hynek (2012b) is shown in light blue and labeled as "Original." The craters that could be measured with MOLA data (PEDR and MEGDR) in this study are shown as a fraction of all the craters in those regions in dark blue and labeled as "New." The fraction of craters analyzable in HRSC DTMs is shown in green—note that only ~7% of the craters in these regions have HRSC DTM coverage to begin with, so only significant deviations below that are meaningful. (For interpretation of the references to color in this figure caption, the reader is referred to the web version of this article.)

Interestingly, these relative diameter cut-offs do not scale with the resolution of the data. For MOLA, this $< 50\%$ point corresponds to craters that are $\lesssim 8$ MEGDR pixels across, while for the HRSC, the $< 50\%$ point is for craters $\lesssim 24$ pixels across. Our hypothesis is that this is due to the nature of the data: MOLA are directly measuring topography, but the DTMs are a derived product based on finding corresponding points on a surface, the difference between them, and determining the vertical distance to the craft based on viewing geometry. The DTM creation has variable success across a single image and relies on interpolation between matched points, while, for HRSC itself, the images used are starting from a lossy compression. Without minimizing the work that goes into deriving each DTM, these stated effects combine to make it less useful pixel-for-pixel relative to the MOLA product.

4.2. Current MEGDR analysis compared with previous MEGDR analysis

While the new topography code described in Section 3 is different from the version used before, neither is any more correct nor incorrect than the other, for they are each measuring different properties. The older version represents more of an average rim height and floor depth while the revised code is designed to pick

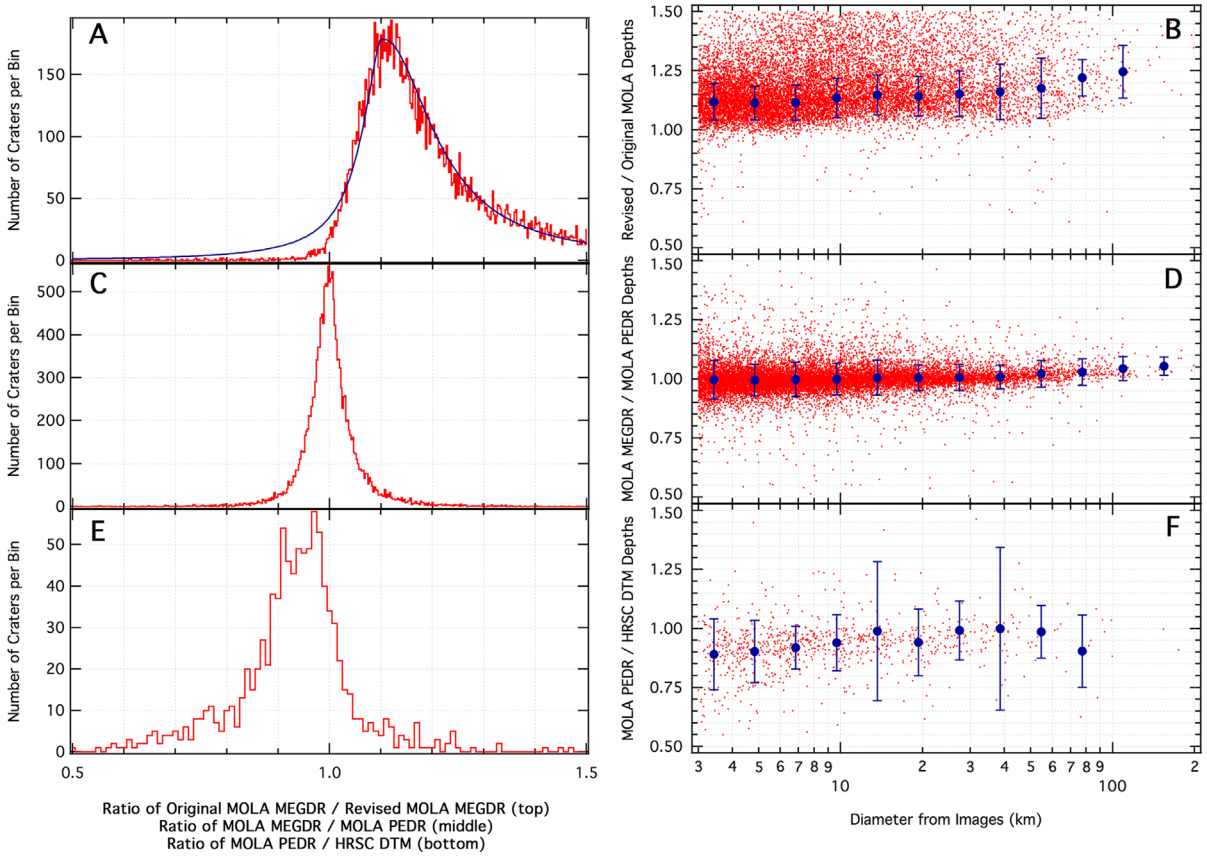

Fig. 4. Panels represent comparison between original and revised topography code with MOLA data (A-B), MOLA MEGDR and PEDR (C-D), and MOLA PEDR with HRSC DTM (E-F) crater rim-floor depths. The left column shows diameter-independent averages, while the right column shows diameter-dependent results with the data (red points) binned (blue points) in $2^{1/2}D$ multiplicative intervals. Panel A shows the results of a piece-wise Lorentzian fit (blue line) as described in Section 4.2; Panel B was binned with the means of a Lorentz fit and standard deviation from Gaussian. (For interpretation of the references to color in this figure caption, the reader is referred to the web version of this article.)

out the highest points along the rim and deepest points of the floor. The two are not inter-relatable (one cannot be used to estimate the other from first principles), but one can examine the overall differences between them for the craters examined. As a specific example, the crater shown in Fig. 2 has a rim-floor depth of 0.98 ± 0.10 km under the old code, and 1.05 ± 0.06 km with the new code from both MEGDR and PEDR data.

The ratio of the new crater depths to old was, on average, 12% larger under the semi-automatic topographic technique. However, there is a large dispersion in these values and it is highly non-symmetric about the mode, which is 1.12 (Fig. 4A). It can be approximately modeled as a two-part Lorentzian. For values smaller than the mode, the γ parameter of the fit is 0.035, while for values larger than the mode, γ is 0.112; the mean of both fits is 1.12. This means that there is a tight distribution with few craters smaller than the mode and an extended distribution with the most craters larger than the mode. As with other parts of the analysis in subsequent sections, this was diameter-dependent (Fig. 4B). If a Lorentz distribution is used to determine the mean values within a diameter bin (Fig. 4B), craters $D \approx 100$ km average 25% deeper, $D \approx 30$–50 km average 16–22% deeper, $D \approx 10$ km average 12% deeper, and $D \approx 5$ km average 11% deeper with the new technique.

4.3. MOLA MEGDR compared with PEDR

One of the primary motivators of this work was to understand how well the gridded MOLA MEGDR represented the vector PEDR data for crater topography. Robbins and Hynek (2012a) performed a *post hoc* statistical test after the majority of data had been gathered, and that study also examined four craters' PEDR and MEGDR results in detail. It was shown that the results were comparable. But, the question remained how those results would bear out on a larger sample size and how they would compare with this revised topography technique.

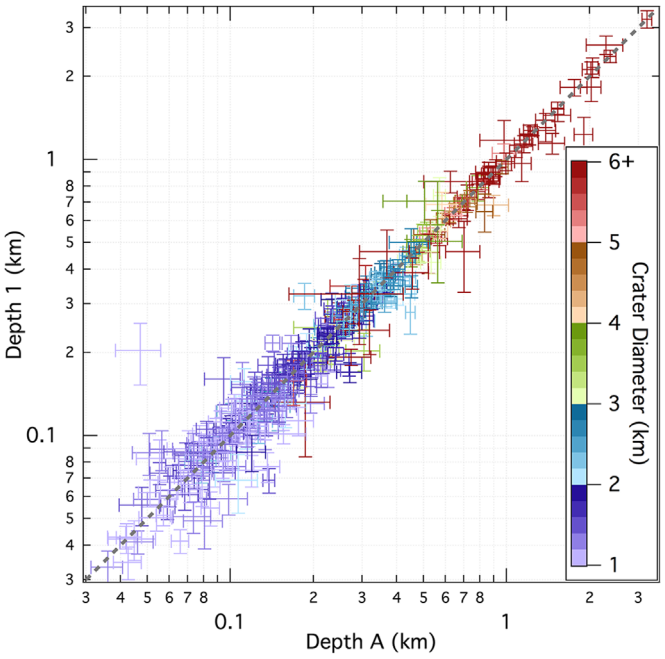

Fig. 5. Five hundred forty-six comparison crater rim-floor depths from different HRSC DTMs of the same craters in the regions of interest. Error bars are the sum of the rim and floor standard deviations. Since no given DTM has precedence over another, they are labeled as "Depth 1" and "Depth A." Colors represent crater diameters, while the dark red is any crater $D \geq 5.8$ km. The dashed diagonal line represents a 1:1 agreement, and the very good and diameter-independent clustering around it shows that the HRSC DTMs are self-consistent.

To this end, we examined the differences between craters' rim-floor depths analyzed with MOLA MEGDR and PEDR data. They were first compared regardless of crater diameter. The ratio of rim-floor depths from MEGDR was taken relative to rim-floor PEDR depths. A histogram is shown in Fig. 4C, and the sample size of craters examined is $N = 16{,}508$. While the distribution is a Lorentzian, the core can be approximated as a Gaussian and hence a standard deviation calculated. The mean is $99.6 \pm 3.0\%$, indicating that, on average, PEDR data result in slightly deeper craters, but this is minimally significant. Expanding into diameter space, Fig. 4D shows the ratio versus crater diameter, where a ratio of 1.0 would be parity between MEGDR and PEDR results. There is a very small diameter dependence where craters $D \approx 5$ km are deepest in PEDR relative to MEGDR, but the $\pm\sigma$ bars overlap 1.0 in all diameter bins; the maximum difference is $\mu = 3.0\%$. For the very largest craters ($D \gtrsim 100$ km), MEGDR is deeper than PEDR by $\sim$4 to 5%. Thus, MEGDR and PEDR data are comparable for the most part, validating their use for this purpose by researchers seeking to use a simpler dataset that is generally easier to utilize.

4.4. HRSC self-consistency analysis

The HRSC instrument has imaged the majority of Mars as of the time of this writing, and some areas have been imaged multiple times. Some of the 124 DTMs used in this work have regions of overlap, and within those, 1460 craters from our database were duplicated. Of the duplicated craters, 546 were analyzable in at least two images, and of those, eight had depths calculated in three images. The rim-floor crater depth from one DTM is graphed against the rim-floor depth derived in the other DTM in Fig. 5, and error bars are the sum of the standard deviations of the rim and floors as described in Section 3. There is very good agreement between craters done in different DTMs, indicating that these data are reliable for this type of depth study, or at least they are self-consistent. The largest outlier is the 154-km Gale Crater, where the western half was observed and measured in one DTM and the eastern half in another. Since the floor of Gale crater is not radially symmetric, different depths were found.

4.5. MOLA PEDR compared with HRSC DTMs

An analysis similar to MOLA MEGDR versus PEDR (Section 4.3) was completed for PEDR versus the HRSC DTMs (PEDR were used because the DTMs' results are slightly closer to PEDR than MEGDR). The craters were first compared regardless of crater diameter. The ratio of rim-floor depths from MOLA PEDR was taken relative to rim-floor HRSC DTM depths. A histogram is shown in Fig. 4E, and the sample size of craters is $N = 974$. The mean is $93.9 \pm 6.5\%$, indicating that, on average, PEDR data result in somewhat shallower craters with 82% being below parity with HRSC-based rim-floor depths. Expanding this in diameter space, Fig. 4F shows the ratio as a function of crater diameter, where a ratio of 1.0 would be parity between MOLA PEDR and HRSC DTM results. There is a diameter dependence where smaller craters ($D < 10$ km) are up to ≈10% deeper with HRSC-based data, though the $\pm\sigma$ bars overlap 1.0 in all diameter bins. Of questionable statistical significance but visible in the data is a sigmoid distribution where craters $D \gtrsim 10$ km are generally within 1% of parity, but the next-smallest diameter bin falls more than 5% below it, and the smaller diameters continue to drop (this is robust with different binning intervals). Under the assumption that HRSC DTMs are the most accurate dataset of those in this study for craters $D \geq 3$ km, the conclusion from this is that, as a whole, MOLA PEDR data are reliable for craters $D \gtrsim 10$ km ($\sim$30 points along-track), but they can alias depths to be up to 10% shallower at smaller crater diameters.

Table 1
The simple (top line) and complex (bottom line) depth versus diameter power law relationship derived for craters equator-ward of $\pm 40^{\circ}$ latitude. Values from Robbins and Hynek (2012b), calculated using the earlier topography algorithm, are included for comparison in the columns labeled with "(R&H12b)".

	Deepest craters (New)	Deepest craters (R&H12b)	All craters (New)	All craters (R&H12b)
Smp (N=6793)	$d=0.227D^{0.901}$	$d=0.179D^{1.012}$	$d=0.126D^{0.986}$	$d=0.047D^{1.284}$
Cpx (N=842)	$d=0.371D^{0.510}$	$d=0.286D^{0.582}$	$d=0.290D^{0.411}$	$d=0.107D^{0.559}$

4.6. Crater depth Vs. diameter ratio for Mars

One of the primary motivators for determining crater depth is to estimate the "pristine" diameter-dependent crater depth vs. diameter ratio (d/D), a value that is often fit to a power law—a $d=\alpha \cdot D^{\beta}$ model is used here. Morphologically, craters are divided into two primary classes: simple craters, which are concave throughout and are small, versus complex craters which are larger and are primarily characterized by a flat floor or a floor with additional characteristics such as a central peak or ring. Simple craters have a different d/D than complex craters, so different relationships must be derived for each. The diameter at which a crater will transition between the two (the "transition diameter") is generally gravity-dependent, but it can also be affected by material strength in which the crater forms and impactor velocity (Pike, 1980, 1988; Schultz, 1988; Stewart and Valiant, 2006; Boyce and Garbeil, 2007; Robbins and Hynek, 2012b).

Robbins and Hynek (2012b) performed this analysis in 19 different permutations, determining the average, deepest, and morphologically pristine crater relationships for all of Mars, equatorial latitudes ($<\pm 40^{\circ}$), higher latitudes ($>\pm 40^{\circ}$), northern plains terrain, southern highlands terrain, volcanic terrain, and polar terrain for both simple and complex craters. Such an extensive re-analysis is neither warranted nor possible with the limited HRSC coverage (Fig. 1), but we can re-assess the overall average and deepest crater relationships for the equatorial latitudes.

All craters with depths determined in HRSC data equatorial to $\pm 40^{\circ}$ latitude were extracted along with their morphologic classification from the Robbins and Hynek (2012a) catalog. That catalog only classified crater morphometry for $D\geq 3$ km, but with the transition diameter for Mars at approximately 6 km (Pike, 1980, 1988; Robbins and Hynek, 2012b), all craters $D\leq 3$ km were assumed to be simple for this analysis. Craters were separated into simple and complex groups, and the depths were then binned in diameter space in multiplicative intervals of $2^{1/N}D$ where N was set to 2, 3, and 4 to determine parameter robustness. Within each bin, an overall average was fit (for the "average" technique), and the deepest 5% and 10% were also binned (to test robustness for the "deepest" technique). N per bin was defined as a minimum of three craters; for complex craters, the maximum was $N=21$, while for simple craters, the maximum N was 150 from which average bin values were derived.

In all cases, the fit parameter values varied somewhat, but they were within each others' uncertainties for each parameter. The value that varied the most was the exponent of the complex craters when determining the deepest values—this was likely due to the small N binned within each diameter interval contributing to the noise level. Because the values were generally robust, a weighted mean was taken for each, and they are summarized in Table 1. Besides being a revision to Robbins and Hynek (2012b), these results also extend the simple crater d/D relationship to $D=1$ km craters. In all cases, the result of these new data are to deepen the craters (increase the amplitude coefficient, α, of the fit), as would be expected from the preceding analysis. Additionally, in all cases, the exponent of the power-law, β, decreased slightly—by 10% for the deepest craters method and by 30% for the overall average method. Physically, this means that smaller craters are deeper relative to what was determined previously, and while larger craters are deeper than smaller craters, the increase in depth is not as rapid; this is consistent with the offsets between MOLA and HRSC data as detailed above.

Three others have published global values from models similar to the "deepest" method—Garvin et al. (2003), whose results agree very well with these but were a relatively poor match for Robbins and Hynek (2012b); Boyce and Garbeil (2007), whose results more closely matched the previous work and so match this more poorly; and Tornabene et al. (2013) whose data for 20 deep complex craters also match the results here well. Stewart and Valiant (2006) also published depth results for various Martian terrain based on a few dozen craters, and these data are in reasonable agreement with their results, as well. Because of a general lack of geophysical meaning, few have published overall averages in the literature. The main was Stepinski et al. (2009) whose results for simple craters are a poor match for either this or the previous work, while the results for complex craters for both the amplitude and exponent fall almost exactly between our previous and new results. Clearly, as we emphasized in Robbins and Hynek (2012b), defining "the answer" will not be possible, and this work should be considered as coming incrementally closer to the Martian crater d/D function when crater rim height and floor depth are defined as the highest points along the rim and deepest within the floor.

5. Discussion

To answer the basic question of, "To what crater diameter are MOLA data reliable to derive topography on Mars?" they are reliable for diameters $D\gtrsim 10$ km, though in our opinion, only ≈90% of these craters have enough MOLA coverage to even be analyzed. HRSC data at 50 m/px are likely reliable for at least craters $D\gtrsim 2$ km (there is a discontinuity in the d/D slope for $D\lesssim 1.5$ km that could be due to HRSC's own aliasing, but it is inconclusive at this time). And, while PEDR data are more accurate and precise than MEGDR, the variation between the two averages no more than 0.5%, which is within the variation for rim height, and it is generally diameter-independent.

Within and beyond this, one also needs to examine what is meant by a crater "rim" to determine whether a 1% offset, 3% offset, or even 10% offset is meaningful. Typically on other planets with most forms of remote sensing data available, one defines this as the highest point of the visible crater rim (Turtle et al., 2005). Ideally, craters form with a uniform rim height, but practically speaking, this is far from the case in a real environment, and modification processes can significantly alter the fresh rim. Take, for example, Meteor Crater, the best preserved sizable impact crater on Earth, about 55 km from Flagstaff, AZ, USA. Its diameter is approximately 1.3 km. It was imaged with LiDAR in 2010 (Palucis and McEnulty, 2010), and from a 50,000,000-count point cloud subset, a 1 m/px dataset was derived and analyzed per Section 3. The rim elevation from 4274 rim points before the $<\mu$ rejection was 1733 ± 4.6 m, but it ranged between 1716 and 1751 m above sea level (the actual rim trail around the crater has a similar range, 1717–1749 m, as measured *in situ* by the authors). After $<\mu$ rejection, the height was

1738 ± 4.6 m above sea level, and given the floor's elevation, the overall crater depth was found to be 175 ± 5 m. That physical 35-m variation along the rim, however, is a variation of 20% of the overall crater rim-floor depth—and this is for a comparatively pristine terrestrial crater. It also is likely an artificially low value because it is estimated that Meteor Crater has experienced at least 10 m in rim erosion in its ~50,000-year history. With this in mind, we strongly advise all researchers when performing crater topographic examination to clearly define terms: what is actually meant by "rim" and "floor" and exactly how they are measured. The details can significantly affect the outcome as described in this paragraph and Section 4.2. It is also why we conclude that a ~0.5% offset between MOLA MEGDR and PEDR results is insignificant.

There are numerous implications from our results that have a bearing on the broader issue of dataset reliability for those being generated for the terrestrial planets. A significant question relates to the inter-reliability and actual limits to these measurements as more spacecraft are returning data in a variety of formats from different solar system bodies. For example, currently in orbit of Mercury is the *MESSENGER* spacecraft. One main goal is to create a global topographic map of the planet. However, the craft is in a highly elliptical orbit. It contains a laser altimeter (Mercury Laser Altimeter, MLA (Cavanaugh et al., 2007) that is tasked with creating a dataset for the northern hemisphere, but the laser cannot operate in the southern hemisphere due to the large apoapsis centered near the Hermean south pole. *MESSENGER* contains a camera system (Mercury Dual Imaging System, MDIS (Hawkins et al., 2007) tasked with generating a DTM-based topographic dataset for the southern hemisphere, and the two will be tied together near the equator where they both overlap (Solomon et al., 2007). Even if the gridded results from this dataset are matched well at the equator and appear uniform overall (i.e., 300 m/pix, or 1/128°), it is very likely from the work shown here that the actual utility of the set will vary, where the DTMs will not be as useful for small features as the laser data. With the HRSC DTMs assisted by MOLA to help with accuracy, and MDIS DTMs lacking that ability except for a few degrees latitude of overlap, issues may be even more significant.

Similarly, the *Lunar Reconnaissance Orbiter* has both a laser altimeter (Lunar Orbiter Laser Altimeter, LOLA) and wide- and narrow-angle cameras (*Lunar Reconnaissance Orbiter* Camera, Wide-Angle Camera (LROC WAC), and Narrow-Angle Camera (LROC NAC)) (Chin et al., 2007). The craft entered orbit in 2009 and already the LOLA team has made available over 6.0 billion valid datapoints as of Spring 2013 (K. Bennett, pers. comm.). The instrument functions similarly to MOLA, except that it is upgraded with five lasers per pulse, a faster pulse rate, less beam dispersion, smaller footprints (and the craft is in a lower orbit), and better across-track spacing (more orbits around a smaller body). The team has also released gridded datasets and will continue to update these until the instrument fails or the mission ends. Meanwhile, the LROC team released in 2011 the first version of a 100 m/px global DTM based on WAC data, since LROC WAC provides near-complete lunar imaging once per terrestrial month (as of June 2012, they had fully imaged the Moon, at a variety of solar incidence angles, 33 times). While both LROC DTMs and LOLA gridded products are in their early stages, as one approaches the ~10-pixel level, one can already start to see the same effects detailed in this paper for Mars where the DTMs fail to resolve fine topographic features before the laser data (Robbins, unpublished work). This is an important bias of which people should be aware as these datasets become more refined and more widespread in use.

We plan to continue to re-measure craters in MOLA topography with the new topography code and to analyze new HRSC DTMs at 1183° per pixel as they become available. If *Mars Reconnaissance Orbiter* ConTeXt Camera (CTX) DTMs become publicly available, or as we find time to generate our own, we also plan to explore the limits of the HRSC resolution (CTX data have native pixel scales of ~5.5 to 7.5 m/px). However, we expect the specific results of this analysis to hold up: MOLA data can be used accurately for craters down to $D \approx 10$ km, but results will be aliased at smaller diameters. But, the actual number of pixels at which the laser-based MOLA data begins to fail is fewer than the HRSC stereopair-based DTMs, indicating that attempts to use the two interchangeably with comparable-resolution datasets will lead to inconsistencies. For this reason, we recommend that researchers compare the two, where possible, before relying upon one or the other.

Acknowledgments

The authors thank one anonymous reviewer for their comments and S.T. Stewart-Mukhopadhyay for providing a synthetic crater dataset used in this work. Support for this work was NASA MDAP Award NNX10AL65G. LiDAR data acquisition and processing completed by the National Center for Airborne Laser Mapping (NCALM - http://www.ncalm.org). NCALM funding provided by NSF's Division of Earth Sciences, Instrumentation and Facilities Program, EAR-1043051.

References

Boyce, J.M., Garbeil, H., 2007. Geometric relationships of pristine Martian complex impact craters, and their implications to Mars geologic history. Geophysical Research Letters 34, L16201, http://dx.doi.org/10.1029/2007GL029731.

Cavanaugh, J.E., 18 co-authors, 2007. The Mercury laser altimeter instrument for the MESSENGER mission. Space Science Review 131, 451–479, http://dx.doi.org/10.1007/s11214-007-9273-4.

Chapman, C.R., Jones, K.L., 1977. Cratering and obliteration history of Mars. Annual Review of Earth and Planetary Sciences 5, 515–540.

Chin, G., 16 co-authors, 2007. Lunar Reconnaissance Orbiter overview: the instrument suite and mission. Space Science Review 129, 391–419, http://dx.doi.org/10.1007/s11214-007-9153-y.

Davis, P.A., Soderblom, L.A., 1984. Modeling crater topography and albedo from monoscopic Viking Orbiter images 1. Methodology. Journal of Geophysical Research 89 (B11), 9449–9457, http://dx.doi.org/10.1029/JB089iB11p09449.

Garvin, J.B., Sakimoto, S.E.H., Frawley, J.J. 2003. Craters on Mars: Geometric properties from gridded MOLA topography. International Conference on Mars 6, Abstract #3277.

Gwinner, K., Scholten, F., Preusker, F., Elgner, S., Roatsch, T., Spiegel, M., Schmidt, R., Oberst, J., Jaumann, R., Heipke, C., 2010. Topography of Mars from global mapping by HRSC high-resolution digital terrain models and orthoimages: characteristics and performance. Earth and Planetary Science Letters 294, 506–519, http://dx.doi.org/10.1016/j.epsl.2009.11.007.

Hawkins III, S.E., 24 co-authors, 2007. The Mercury dual imaging system on the MESSENGER spacecraft. Space Science Review 131, 247–338, http://dx.doi.org/10.1007/s11214-007-9266-3.

Jaumann, R., 26 co-authors, 2007. The high-resolution stereo camera (HRSC) experiment on Mars Express: instrument aspects and experiment conduct from interplanetary cruise through the nominal mission. Planetary and Space Science 55, 928–952, http://dx.doi.org/10.1016/j.pss.2006.12.003.

Neukum, G., Jaumann, R., 2004. HRSC: the High Resolution Stereo Camera of Mars Express. In: Wilson, A., Chicarro, A. (Eds.), 1240. ESA Special Publications, pp. 17–35.

Neumann, G.A., Abshire, J.B., Aharonson, O., Garvin, J.B., Sun, X., Zuber, M.T., 2003a. Mars Orbiter Laser Altimeter pulse width measurements and footprint-scale roughness. Geophysical Research Letters 30 (11), 1561, http://dx.doi.org/10.1029/2003GL017048.

Neumann, G.A., Lemoine, F.G., Smith, D.E., Zuber, M.T., 2003b. The Mars Orbiter Laser Altimeter archive: final precision experiment data record release and status of radiometry. Lunar and Planetary Science XXXIV, Abstract #1978.

Palucis, M., McEnulty, T. 2010. Meteor Crater, AZ: a terrestrial analog to study gully formation on Mars. NCALM Report. 10.5069/G9V40S4C.

Pike, R.J., 1976. Crater dimensions from Apollo data and supplemental sources. Moon 15, 463–477, http://dx.doi.org/10.1007/BF00562253.

Pike, R.J., 1977. Apparent depth/apparent diameter relation for lunar craters. Proceedings of the Lunar and Planetary Science Conference 8, 3427–3436.

Pike, R.J. 1980. Control of crater morphology by gravity and target type: Mars, Earth, Moon. Proceedings of the Lunar and Planetary Science Conference 11, 2159–2189.

Pike, R.J., 1988. Geomorphology of impact craters on Mercury. In: Vilas, F., Chapman, M.S., Matthews, M.S. (Eds.), Mercury, 1988. University of Arizona Press, pp. 165–273 0-8165-1085-7.

Robbins, S.J., Hynek, B.M., 2012a. A New Global Database of Mars Impact Craters ≥1 km: 1. Database Creation, Properties, and Parameters. Journal of Geophysical Research 117, E05004, http://dx.doi.org/10.1029/2011JE003966.

Robbins, S.J., Hynek, B.M., 2012b. A new global database of Mars impact craters ≥1 km: 2. Global Crater properties and regional variations of the simple-to-complex transition diameter. Journal of Geophysical Research 117, E06001, http://dx.doi.org/10.1029/2011JE003967.

Schultz, P.H., 1988. Cratering on Mercury: A Relook. In: Vilas, F., Chapman, C.R., Matthews, M.S. (Eds.), Mercury, 1988. University of Arizona Press, pp. 274–335 0-8165-1085-7.

Smith, D.E., 23 colleagues, 2001. Mars Orbiter Laser Altimeter: experiment summary after the first year of global mapping on Mars. Journal of Geophysical Research 106, 23,689–23,722, http://dx.doi.org/10.1029/2000JE001364.

Solomon, S.C., McNutt Jr., R.L., Gold, R.E., Domingue, D.L., 2007. MESSENGER mission overview. Space Science Review 131, 3–39, http://dx.doi.org/10.1007/s11214-007-9247-6.

Stepinski, T.F., Mendenhall, M.P., Bue, B.D., 2009. Machine cataloging of impact craters on Mars. Icarus 203, 77–87, http://dx.doi.org/10.1016/j.icarus.2009.04.026.

Stewart, S.T., Valiant, G.J., 2006. Martian subsurface properties and crater formation processes inferred from fresh impact crater geometries. Meteoritics & Planetary Science 41 (10), 1509–1537, http://dx.doi.org/10.1111/j.1945-5100.2006.tb00433.x.

Tornabene, L.L., Ling, V., Osinski, G.R., Boyce, J.M., Harrison, T.N., McEWen, A.S. 2013. A revised global depth-diameter scaling relationship for Mars based on pitted impact melt-bearing craters. Lunar & Planet Science Conference, 44, Abstract #2592.

Turtle, E.P., Pierazzo, E., Collins, G.S., Osinski, G.R., Melosh, H.J., Morgan, J.V., Reimold, W.U., 2005. Impact structures: what does crater diameter mean? In: Kenkmann, T, Hörz, F., Deutsch, A. (Eds.), Large Meteorite Impacts III. Geological Society of America Special Paper, pp. 1–24 384.

Zuber, M.T., Smith, D.E., Solomon, S.C., Muhleman, D.O., Head, J.W., Garvin, J.B., Abshire, J.B., Bufton, J.L., 1992. The Mars Observer laser altimeter investigation. Journal of Geophysical Research 97 (E5), 7781–7797, http://dx.doi.org/10.1029/92JE00341.